Ⓔ

Shallow V_S Imaging of the Groningen Area from Joint Inversion of Multimode Surface Waves and H/V Spectral Ratios

by Zack Spica, Mathieu Perton, Nori Nakata, Xin Liu, and Gregory C. Beroza

ABSTRACT

The Groningen gas field in the northern Netherlands is subject to production-induced earthquakes and has quickly become one of the seismologically best-instrumented areas on Earth. Accurate quantification of seismic hazard from potential future earthquakes requires accurate shallow velocity structure for ground-motion prediction. Toward this end, we present a shear-wave velocity model developed through the joint inversion of multimode Love- and Rayleigh-wave dispersion curves (DCs) and H/V spectral ratio (HVSR) measurements. We obtain local DCs from azimuthally averaged frequency–time analysis of the cross correlation of the ambient seismic field (ASF) between pairs of stations. HVSR is measured at each station from the directional energy density, that is, the autocorrelation of the ASF for all components. We simultaneously fit these observables at each station of the dense Loppersum array to infer a 1D velocity model from the surface to a depth of ~900 m. In the frequency range considered (~1–7 Hz), Rayleigh-wave DCs show high modal complexity, which makes clear identification of the modes challenging and leads us to downweight their contribution to the result. Fundamental- and higher-mode Love-wave dispersion is much clearer. We find good agreement between our model and independently derived models of shallow structure, which validates our approach and supports the value of HVSR analysis as a tool to map subsurface properties.

Electronic Supplement: Frequency–time diagrams, theoretical k_x, omega diagrams, example joint inversion for site 235587, and example of horizontal-to-vertical (H/V) spectral ratio (HVSR) at station site 235587.

INTRODUCTION

The Groningen area in the northern Netherlands (Fig. 1a) hosts one of the world's largest onshore natural gas fields. Since the beginning of its exploitation in 1963, it has been an important source of energy for western Europe. Its long-term exploitation has led to compaction at reservoir depth, and the resulting subsidence induces earthquakes (van Thienen-Visser and Breunese, 2015). In response to recent concerns about induced seismicity in this region, the field operator, Nederlandse Aardolie Maatschappij [NAM], along with the Royal Netherlands Meteorological Institute (KNMI) are leading an extensive data acquisition and modeling program to quantify seismic hazard and risk in the region (e.g.,van Elk *et al.*, 2017). Part of this response includes the construction of a permanent shallow borehole microseismic network (the G-array; Fig. 1b) and the deployment of temporary nodal seismic experiments involving up to ~415 three-component sensors (e.g., Spica *et al.*, 2018).

Site characterization is an essential component of integrated hazard assessment in the Groningen area (Bommer *et al.*, 2017; Rodriguez-Marek *et al.*, 2017). The deltaic deposits covering most of the area with an average shear-wave velocity of about 200 m/s are expected to have an appreciable influence on ground motions by increasing the amplitude and duration of shaking and by responding nonlinearly to incident seismic waves in the event of strong shaking. Since the installation of the G-array in late 2015 (Fig. 1b), several studies have developed region-specific models of the subsurface, with the goal of reducing epistemic uncertainty in ground-motion prediction models (Hofman *et al.*, 2017; Kruiver *et al.*, 2017; Spica, Perton *et al.*, 2017; Zhou and Paulssen, 2017; Noorlandt *et al.*, 2018). This study pursues this same objective through a novel technique to develop a high-resolution near-surface V_S model of the Loppersum area (Fig. 1c), which currently has the highest induced-seismicity rate observed in the Groningen region.

Ambient seismic field (ASF) tomography (Shapiro *et al.*, 2005) is a widely used method to image seismic velocities at regional (e.g., Sabra *et al.*, 2005; Stankiewicz *et al.*, 2012; Spica, Legrand, *et al.*, 2015; Spica, Perton, and Legrand, 2017) or continental scales (e.g., Lin *et al.*, 2008; Spica *et al.*, 2016). The method relies on the cross correlation of ASF recorded

doi: 10.1785/0220180060

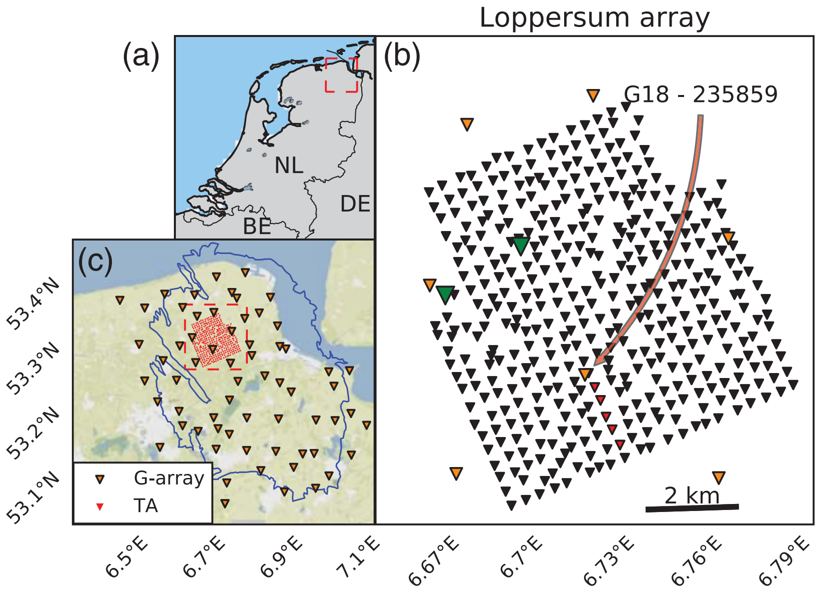

▲ **Figure 1.** (a) Location of the Groningen gas field in the northern Netherlands. (b) Map view of the Groningen gas field area. Blue contour shows the boundary of the gas field. Orange triangles depict the shallow borehole sites of the G-array, which consists of 70 accelerographs at the surface collocated with a borehole in which three to four geophones are installed at depth intervals of 30, 50, or 75 m. Small red triangles depict stations of the Loppersum array, reported as Transportable Array (TA) in the legend. (c) Loppersum array (black triangles) and the surrounding stations of the G-array (orange triangles). The two green triangles depict the deep borehole locations: ZRP (western) and SDM (eastern). The line of five stations close to the shallow borehole G18 are shown in red. Inversion results for these stations are highlighted in Figure 3. A detailed description of some of the seismic arrays in the Groningen area is provided in Spica *et al.* (2018).

at different locations to approximate the Green's function between seismic sensors (Shapiro and Campillo, 2004). The frequency bandwidth of the retrieved Green's functions (typically 0.05–0.5 Hz) depends both on the source characteristics and the interstation distance. Because high frequencies attenuate quickly with distance, most ASF results lack resolution of the near surface. Small-aperture arrays, with short interstation distances, are required to constrain the near-surface velocity structure. Arrays with sufficiently small interstation distances can be used to recover high-frequency dispersion curves (DCs) that constrain the local 1D velocity structure for the upper few hundred meters, and subsets of stations forming small-aperture subarrays can be used to achieve good horizontal resolution.

The possibility of retrieving the Green's function from the average time-domain correlation of ambient field records has led to a new interpretation of Nakamura's H/V spectral ratio (HVSR) measurements (Nakamura, 1989). Sánchez-Sesma *et al.* (2011) used the diffuse field assumption (DFA) to link the H/V of the autocorrelated signal (i.e., the directional energy densities in Perton *et al.*, 2009) to the ratio of the imaginary parts of the 1D Green's functions. This formulation naturally allows for inversion of the structure at a site, and the inversion of the full spectrum of the H/V ratio has emerged as a powerful technique that has been applied to diverse data sets and geological settings (Salinas *et al.*, 2014; Spica, Caudron, *et al.*, 2015; Lontsi *et al.*, 2015, 2016; Rivet *et al.*, 2015; García-Jerez *et al.*, 2016; Piña-Flores *et al.*, 2016; Perton *et al.*, 2017; Wu *et al.*, 2017). It has also proven its potential to give a reliable velocity model of the shallow subsurface using shallow borehole observations from the G-array (Spica, Perton, *et al.*, 2017).

A drawback of the method, however, is that H/V at the surface is insufficient to characterize shallow properties uniquely because layer velocities and thicknesses trade off and lead to a similar HVSR (Piña-Flores *et al.*, 2016). Independent information such as surface-wave DCs (Scherbaum *et al.*, 2003; Lontsi *et al.*, 2016; Piña-Flores *et al.*, 2016) or HVSR measurements recorded at different depths (Lontsi *et al.*, 2016; Spica, Perton, *et al.*, 2017) are two possible strategies for reducing this nonuniqueness. DCs extracted from the ASF are sensitive to the absolute velocity; however, they suffer from their own nonuniqueness, because the broad sensitivity kernels of surface waves sample a wide range of depths, depending on their frequency. In contrast, HVSR is primarily sensitive to sharp shear-wave velocity contrasts and vertical travel times, offering a complimentary measurement.

We use data from the Loppersum array, which is the first phase of the temporary three-component nodal deployment (Fig. 1c), to characterize the subsurface with high resolution using a novel joint inversion of HVSR and Love-wave plus Rayleigh-wave dispersion, as measured from seismic interferometry with small-aperture array techniques. The ASF in the Groningen area is remarkably rich in higher-mode surface waves (Spica *et al.*, 2018). Although higher modes are often considered as a problem and then avoided, they provide strong constraints on the velocity model because they are sensitive to different depths than the fundamental mode at the same frequency (e.g., Tomar *et al.*, 2018). In the specific case of Groningen, we show that Love-wave DCs are more clearly expressed than Rayleigh-wave DCs, which leads us to downweight the contribution of the latter in our joint inversion.

We construct the velocity model in three steps. First, we extract the multimode group velocity DCs for Rayleigh and Love waves at each position from azimuthally averaged cross correlations for small subarrays. Second, we compute HVSR at each station from its directional energy density. Third, we fit the three sets of observables at each station of the array to constrain the local shear-wave velocity structure from the surface to a depth of ~900 m. Finally, we reconcile the resulting 1D-layered profiles into a velocity model suitable for ground-motion prediction at Groningen.

DATA

The Loppersum array (Fig. 1c) is composed of 415 temporary three-component stations with 5 Hz natural frequency almost evenly spaced at ~350 m. Stations were deployed for 45 days (Julian days 284 to 329, 2016) around the town of Loppersum. To compute the cross-correlation functions, we used the entire available data set. HVSRs (see HVSR Analysis section) were computed with 24 hrs of data that have been observed to be long enough for their convergence in the frequency range analyzed in this study (Spica, Perton, and Beroza, 2017).

AMBIENT SEISMIC FIELD CROSS CORRELATIONS

We obtained cross-correlation functions by computing power-normalized cross correlations (cross coherence) between all receiver pairs in the frequency domain (e.g., Nakata *et al.*, 2013). Prior to correlation, we removed instrument response and then computed the vertical–vertical (ZZ) component along with the radial–radial (RR) and the transverse–transverse (TT) cross correlations, for which we applied a tensor rotation (Lin *et al.*, 2008). Examples of these correlations are shown and discussed in Spica *et al.* (2018).

Surface-Wave Dispersion Analysis

To characterize surface-wave propagation, we employ the frequency–time analysis (FTAN; e.g., Dziewonski *et al.*, 1969; Levshin *et al.*, 1989), which is widely used to estimate group velocity and DCs from interferograms (Bensen *et al.*, 2007). At each station, we use all available correlations within a radius of 600 m and average over FTAN diagrams between each station pair to suppress the azimuthal dependency. We individually apply FTAN to the ZZ, RR, and TT components of the correlation functions.

Typically, we expect the fundamental mode of the surface wave to be expressed most energetically as the global maximum at each frequency in the FTAN diagrams. Curves with distinctly irregular behavior might either be rejected using formal criteria or smoothed through small glitches by selecting realistic local rather than global absolute maxima (e.g., Bensen *et al.*, 2007). This approach can be biased by osculation (touching) of the fundamental and higher-mode DCs, by scattered arrivals, or by glitches and jumps due to noise.

The ASF recorded by the Loppersum array is rich in higher modes (up to the second and third higher mode for the Rayleigh and Love waves, respectively) as observed in the FTAN diagrams (Fig. 2). To avoid incorrect assignment of the group velocities and to take advantage of all possible modes, we consider all local maxima rather than focusing the global maximum. We obtain a series of different points, some of which are related to surface-wave dispersion, while others are artifacts. Our approach is to consider all of them in the inversion process to fit as many modes as possible and by doing so to improve constraints on the depth dependence of the velocity model. Examples of FTAN diagrams with multimaxima selection are shown in Figure 2 and Ⓔ Figure S1 (available in the electronic supplement to this article).

As observed in several studies (e.g., Lin *et al.*, 2008; Spica, Perton, and Legrand, 2017), the surface waves observed in the TT correlations are Love waves, whereas both the ZZ and RR correlations contain Rayleigh waves. If the medium is homogeneous and isotropic, both ZZ and RR should give similar results. In our data, the small differences between ZZ and RR FTAN diagrams (Ⓔ Fig. S1) are likely due to the different strength of excitation between the components, local lateral heterogeneities, and/or the presence of body waves in the small-offset correlations (Spica *et al.*, 2018). To reduce these effects, we stack the ZZ and RR diagrams (Fig. 2 and Ⓔ Fig. S1c). As shown in Ⓔ Figure S1c, this enhances the quality of the analysis because it gives a clearer identification of the multimode DCs with more continuous lines and fewer glitches (e.g., Campillo *et al.*, 1996).

A striking feature in Figure 2 is that the modal content of the Rayleigh waves appears more complex than that of the Love waves. To understand this behavior, we analyzed the expected surface-wave dispersion based on the velocity model of Kruiver *et al.* (2017) at borehole G18 site (Ⓔ Figs. S2 and S3). The velocity model is shown in the first column in Figure 3. As shown in the theoretical k_x, ω diagram of Ⓔ Figure S2, several Rayleigh modes are present, but they appear sporadically in the FTAN diagram because their energy is distributed over at least three first higher modes. Because $U = (\partial\omega/\partial k_x)$, Ⓔ Figures S2 and S3 cannot be expressed directly in the U domain; however, the energy of the modes can be identified, and points of osculation (touching) are apparent. In the U domain (Fig. 2 and Ⓔ Fig. S1), the osculation points are clearly identifiable through the complex interference pattern of the modal energy maxima. The fundamental mode appears for frequencies higher than 3 Hz, the first overtone from 2.5 to 3.5 Hz, and the second higher mode from 1 to 3 Hz (Fig. 2 and Ⓔ Fig. S1). In contrast, the fundamental Love-wave mode is expected to be the most energetic for the entire spectrum and is well separated from the higher modes (Ⓔ Fig. S3). *A posteriori* analysis of the multimode DC in the (U,f) domain based on one velocity model obtained from our inversion scheme shows similar characteristics. In Ⓔ Figure S4, Love-wave DC shows more-separated fundamental and first modes, whereas Rayleigh-wave DC shows complex fundamental and first. For both Rayleigh- and Love-wave DC, complex modal patterns are observed for modes higher than the first.

The large number of higher modes and their crossings in the (U,f) domain makes unambiguous identification of particular mode branches challenging, and misidentification of the modes would compromise the accuracy of the surface-wave tomography (e.g., Jay *et al.*, 2012). The local 1D approach considered here, with no *a priori* mode identification, is an alternative that still takes advantage of the depth sensitivity kernel of each mode in the inversion, while attempting to avoid misidentifying modal contributions, to the extent possible.

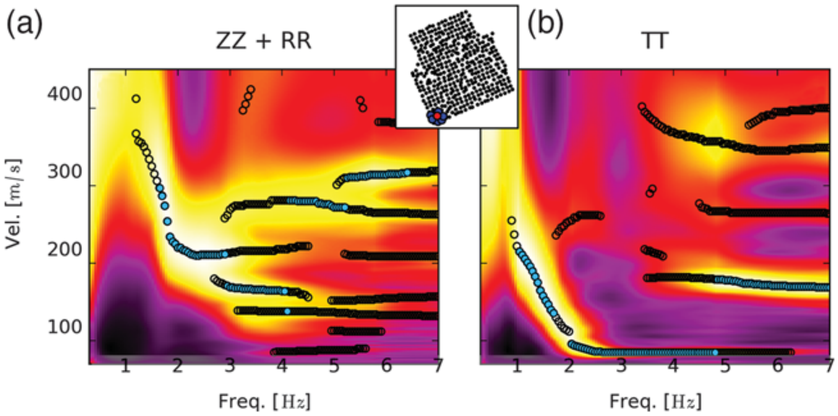

▲ **Figure 2.** Azimuthally averaged frequency–time analysis (FTAN) diagram of the Rayleigh and Love group velocity obtained for Station 235838. The position of the reference station is highlighted as a red dot in the map in the small inset in the upper middle of the figure. Blue dots in the map surrounding the reference station are the other stations used for the analysis within a 600-m radius. Light blue dots in the FTAN diagrams depict the global maximum, and black dots depict local maxima used in the inversion. In this example, the modal content of the Rayleigh wave is clearly more complex than that of the Love wave. Automatic picking of the global maximum would fail to consistently identify the fundamental mode.

HVSR Analysis

Following Sánchez-Sesma *et al.* (2011), we interpret the HVSR recorded at a receiver in terms of the imaginary part of the Green's function:

$$\frac{\mathrm{H}}{\mathrm{V}}(\mathbf{x},\omega) = \sqrt{\frac{\langle|u_1(\mathbf{x},\omega)|^2\rangle + \langle|u_2(\mathbf{x},\omega)|^2\rangle}{\langle|u_3(\mathbf{x},\omega)|^2\rangle}} = \sqrt{\frac{\mathrm{Im}(\mathcal{G}_{11}+\mathcal{G}_{22})}{\mathrm{Im}(\mathcal{G}_{33})}}, \qquad (1)$$

in which $u_i(\mathbf{x},\omega)$ is the displacement spectrum component in the direction i generated by a source applied in direction i when source and receiver are superimposed at x and for frequency $f = \omega/2\pi$. Im refers to the imaginary part of the Green's function ($\mathcal{G}_{ii}$), and the symbol $\langle\rangle$ denotes the average over multiple time windows. Components 1 and 2 are in the horizontal plane whereas component 3 is the vertical. In the first term of equation (1), the $|u_2(\mathbf{x},\omega)|^2$ are the directional energy densities (Perton *et al.*, 2009). They correspond to the average autocorrelations of the ASF, which under a DFA are proportional to the imaginary part of the Green's function. They are therefore treated as classical ASF cross correlations but for the special case when the source and receiver are coincident. Accordingly, we apply spectral whitening to enhance equipartitioning of the wavefield (e.g., Bensen *et al.*, 2007; Spica, Caudron, *et al.*, 2015; Perton *et al.*, 2017; Spica, Perton, *et al.*, 2017). Because several sources can act in different frequency bands, the whitening consists of normalizing the signals by the source energies computed in each time window (i.e., source deconvolution) and in several frequency bands as in Perton *et al.* (2017). In addition to the whitening, Spica *et al.* (2018) showed that high-frequency (> 1 Hz) ASF at Groningen approximates equipartioning in the near surface, making the DFA pertinent for this study.

Equation (1) requires that the averaging is performed separately for each component, so in this respect the procedure differs from the usual HVSR method (Nakamura, 1989). The average is computed on the spectra obtained over one day of continuous data that are windowed into sections of 100 s duration with an overlap of 20%. Each time window is de-meaned, detrended, and band-pass filtered from 0.1 to 10 Hz. Examples of HVSRs along a line of sensors are shown in Figure 3.

Attenuation might be a limitation for a field to become diffuse and then equipartitioned. Several studies have shown this limitation for cross correlation with large interstation distance (e.g., Lawrence and Prieto, 2011). However, for HVSR the interstation distance is null, and the attenuation has a similar effect on waves in all directions. Provided that there are sufficient nearby sources of noise, attenuation should not be a strong limitation. Furthermore, Perton and Sánchez-Sesma (2014) have shown theoretically that, in the presence of attenuation, the autocorrelation is proportional to the Im[$\mathcal{G}$] for the same media but without attenuation. In this contribution, the attenuation is not considered but would be an interesting direction for future research.

1D JOINT INVERSION

In the second term of equation (1), the Im($\mathcal{G}_{ii}$) components are associated with the shallow local structure, which we approximate locally with a horizontally layered geometry having material properties that vary only with depth. Among the several methods that exist to compute HVSR under the DFA (e.g., García-Jerez *et al.*, 2016; Perton and Sánchez-Sesma, 2016; Perton *et al.*, 2017), we use the discrete wavenumber method (Bouchon, 2003), due to its efficiency in solving the forward problem for H/V (Sánchez-Sesma *et al.*, 2011; Perton *et al.*, 2017; Spica, Perton, *et al.*, 2017). For calculation of the theoretical DCs, we follow the scheme presented by Perton and Sánchez-Sesma (2016).

Individually, the inversion of HVSR observations and the inversion of DCs lead to nonunique solutions (e.g., Piña-Flores *et al.*, 2016), but this nonuniqueness can be reduced significantly by joint inversion of both measurements, which exploits the complementary sensitivity of the two types of measurements (e.g., Arai and Tokimatsu, 2004; Parolai *et al.*, 2005; Zor *et al.*, 2010; Dal Moro, 2011; Lontsi *et al.*, 2016; Piña-Flores *et al.*, 2016). HVSR carries information associated with velocity structure, such as strong V_S contrasts, but is weakly sensitive to the absolute velocity. The DCs, on the other hand, are sensitive to absolute velocity variation with depth due to

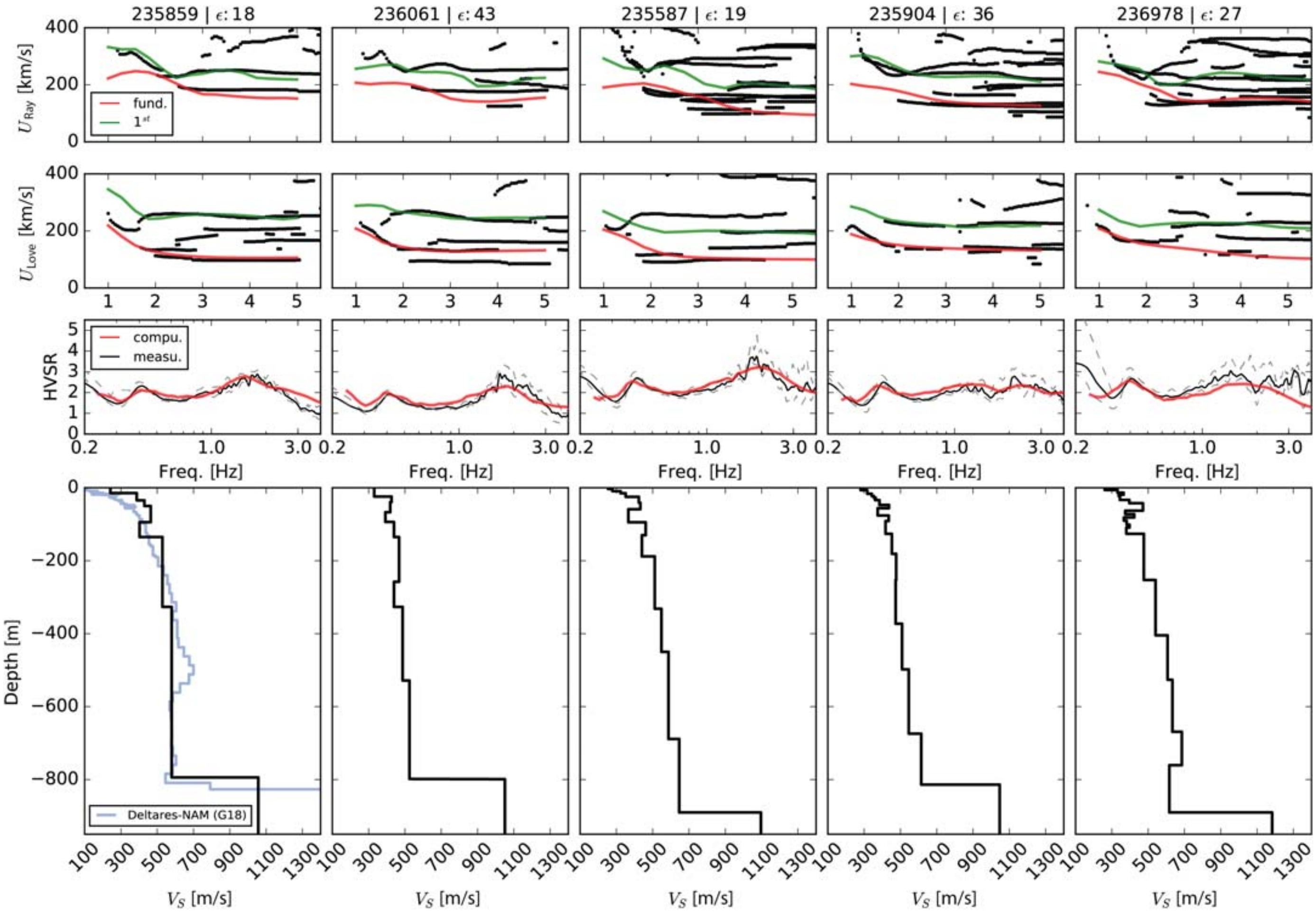

▲ **Figure 3.** Examples of 1D joint inversions at different sites along a line of sensors highlighted in Figure 1. The ID of the stations used is shown on top of each column along with their misfit. From top to bottom of each column we show the multimode Rayleigh dispersion curves (DCs), the multimode Love DCs, the H/V spectral ratio (HVSR), and the estimated velocity model. In the first column of the velocity model panel, we also show the velocity model of Kruiver *et al.* (2017) at borehole site G18.

their frequency dependence (i.e., the sensitivity kernels), but only weakly sensitive to the details of the layering. Furthermore, these two sets of measurements probe slightly different structures. HVSR is a local measurement sampling the structure along an essentially vertical path under the station (e.g., Maupin, 2017), whereas the DCs are expressed across small subarrays. Azimuthally averaged DCs are therefore sensitive to the average of the velocities below the area of all the stations used to compute the local DCs. For laterally heterogeneous structure, the joint inversion yields, at best, a smoothed version of the true velocity structure.

Joint inversion of these two sets of measurements presents several challenges because we must capture the available information in the DCs and HVSR through appropriate weighting. DCs and HVSR have different units, sampling rate, and scaling. Indeed, as shown in Piña-Flores *et al.* (2016), HVSR should be sampled logarithmically to cover a large frequency bandwidth and preserve features. In contrast, DCs are smooth and well suited to linear sampling because the depth sensitivity is proportional to the surface-wave wavelength and hence inversely proportional to frequency. Because the Rayleigh and Love modes are of variable quality and only partially recovered, the number of modes extracted varies from one site to another. As explained in the Surface-Wave Dispersion Analysis section, the modes also interact at osculation points (Ⓔ Fig. S1). Additionally, the bandwidth of the HVSR considered in this study spans almost two orders of magnitude because all HVSRs present peaks at both low and high frequencies (Fig. 3; see Results and Discussion section). HVSR carries information on both shallow (≤ 100 m) and deeper (~800 m) velocity contrasts (e.g., Lin *et al.*, 2012; Spica, Caudron, *et al.*, 2015; Piña-Flores *et al.*, 2016). Proper fitting of the entire spectrum would require a large number of layers to represent correctly the entire velocity profile. The large number of degrees of freedom that result would introduce numerical instabilities in the Green's function calculation (Perton and Sánchez-Sesma, 2016), considerably slow the inversion, and increase the degree of nonuniqueness. To address these issues, we simplify the representation of the velocity structure at each frequency considered during inversion according to the body- and surface-wave wavelengths and reduce it at the depth for which there is no more sensitivity (typically five times the surface-wave wavelength) (Perton *et al.*, 2017). For this reason, at high frequency, only the shallow part of the structure is considered, and at low frequency the very small shallow layers are merged, while conserving propagation time of waves.

Although the joint inversion helps mitigate the nonuniqueness of the problem, the problem remains highly nonlinear with numerous local minima. Perton *et al.* (2017) showed that inverting several positions at the surface simultaneously and constraining the thickness and velocity variation horizontally helps convergence toward a stable solution. Lontsi *et al.* (2015) and Spica, Perton, *et al.* (2017) applied a similar strategy but with stations at depth inside boreholes. In those cases, the degree of heterogeneity and the relatively large sensor spacing (i.e., ~350 m) made this approach infeasible. Definition of an appropriate objective function is an important step in converging to a stable result, and adding constraints, particularly accurate prior information if it is available, can also help reduce the degree of nonuniqueness.

Objective Function

At each station, we use local group velocity DCs for the fundamental- and higher-mode Rayleigh and Love waves, as well as HVSR measurements to estimate shallow velocities and layer thicknesses. Because we carry out no explicit mode identification, the data are not interpolated and only data points close to the frequency sampled by the theoretical curves are considered. This approach is comparable to the one developed by Maraschini *et al.* (2010). After testing several objective functions, we adopted one that includes the fundamental mode and two first higher modes of the surface Rayleigh and Love waves along with the HVSR curve as follows:

$$
\begin{aligned}
&W_{\mathrm{HVSR}} C_{\mathrm{HVSR}} \frac{1}{N^{\mathrm{HVSR}}} \sum_{f_{\min}^{\mathrm{HVSR}}}^{f_{\max}^{\mathrm{HVSR}}} \left(\frac{\mathrm{H}^{\mathrm{computed}}}{\mathrm{V}} - \frac{H^{\mathrm{observed}}}{V} \right)^2 \\
\epsilon^2 = &+ C_{\mathrm{DC}} \frac{1}{N^U} \left[\sum_{f_{\min}^U}^{f_{\max}^U} \sum_{\mathrm{modes}=0}^{1_{\mathrm{Ray}}^{\mathrm{st}}} \mathrm{AF}^2 (U^{\mathrm{observed}} - U^{\mathrm{computed}}) \right. \\
&\left. + \sum_{f_{\min}^U}^{f_{\max}^U} \sum_{\mathrm{modes}=0}^{1_{\mathrm{Lov}}^{\mathrm{st}}} \mathrm{AF}^2 (U^{\mathrm{observed}} - U^{\mathrm{computed}}) \right] \qquad (2)
\end{aligned}
$$

with

$$
F(x) = \begin{cases} x, & \text{if } x < \text{threshold} \\ \text{threshold} & \text{if threshold} < x < 2 \times \text{threshold}. \\ 0, & \text{otherwise} \end{cases}
$$

The normalization factors $C_{\mathrm{HVSR}} = 1/(2e^{-3})$ and $C_{\mathrm{DC}} = 100$ were adjusted so that the summed residuals, respectively, for HVSR and for the DC are almost unitary at the end of the inversion procedure for the best fit. The weight $W_{\mathrm{HVSR}} = 10$ controls the relative influence of HVSR versus DCs in the analysis. Here a higher weight is given to HVSR to result in a better fit of HVSR and to use the DCs as a sort of regularization. N^{HVSR} and N^{DC} are the number of sampled frequencies logarithmically and linearly, respectively. U is the group velocity. The function $F(x)$ excludes spurious arrivals with unrealistic high or low velocities. In the inversion, the weight A given to the fundamental-mode Love wave is twice that given to the Rayleigh (all modes) and Love higher modes. This weighting factor is motivated by the analysis presented in the Surface-Wave Dispersion Analysis section.

Parameterization

The only free parameter considered in our inversion is V_S, the shear-wave velocity. We focus on estimating the shear-wave velocity for several reasons. Both Love- and Rayleigh-wave dispersion are more sensitive to V_S than to other parameters. This is true for HVSR as well (Spica, Caudron, *et al.*, 2015). Moreover, strong ground motion prediction is most strongly dependent on the shear-wave velocity structure, so our focus follows also from our interest in strong ground motion prediction. We need density and *P*-wave velocity too, of course, so we infer the density and the compressional-wave velocity to V_S through empirical relationships of polynomial form (Berteussen, 1977; Brocher, 2005).

We use a harmonically averaged V_S model from Kruiver *et al.* (2017) at Station G18 (Fig. 3, first column) as the starting velocity model for the inversion for all locations. We use a constrained nonlinear optimization procedure (gradient method; Byrd *et al.*, 1999) to minimize the misfit (ϵ); however, when considering a large number of layers, the sensitivity to the parameters decreases. To reduce this effect, the inversion is performed iteratively following the approach described in Spica *et al.* (2016); that is, a layer is inserted between the two layers showing the highest sensitivity (misfit variation for a given velocity variation), and only the parameters of the five surrounding layers (two on each side of the inserted layer) are estimated. This process is repeated iteratively until an acceptable misfit (≤ 45), or a maximum number of layers (20), is reached. Furthermore, to regularize the inversion, we limit the velocity difference to 25% between adjacent layers and to 30% relative to the initial model.

Despite these strong constraints and a good starting velocity model, 41 1D inversions did not succeed in lowering the misfit to an acceptable level (Ⓔ Fig. S5). Most of these show an unrealistic HVSR shape that might be caused by coherent ASF sources, such as transients related to production. Independent H and V clearly show sharp peaks localized around several frequencies (0.5, 1, 1.5, 2, 2.5,... Hz). These peaks generally disappear in the HVSR but not at all locations. Because we believe them to be spurious, we exclude them from further analysis. A map of the repartition of the misfit values over the Loppersum array and the rejected measurements are shown in Ⓔ Figure S5.

RESULTS AND DISCUSSION

Examples of the joint inversion results along a line of sensors starting with Station 235859 is shown in Figure 3. All the HVSRs present similar characteristics and shape, that is, one broad peak around 2–4 Hz that varies strongly in shape and amplitude and two other peaks around 0.15 (Ⓔ Fig. S6) and 0.4 Hz. The 0.15 and 0.4 Hz peaks are extremely stable features over the entire array; however, the 0.15 Hz peak amplitude was not calculated with sufficient confidence to be used during inversion; that is, large amplitude variations were found when varying the number of the time windows during autocorrelation (Ⓔ Fig. S6). The peaks at 0.15 and 0.4 Hz are due to strong impedance contrast at about ~800 depth, which corresponds to the transition between the Lower North Sea Group and the Chalk Group (e.g., Spica *et al.*, 2018). The large peak at 0.15 Hz is due to the surface-wave contribution, and the small peak at 0.4 Hz is due to the body-wave contribution (Piña-Flores *et al.*, 2016). As discussed below, this interface is not well constrained in our inversion.

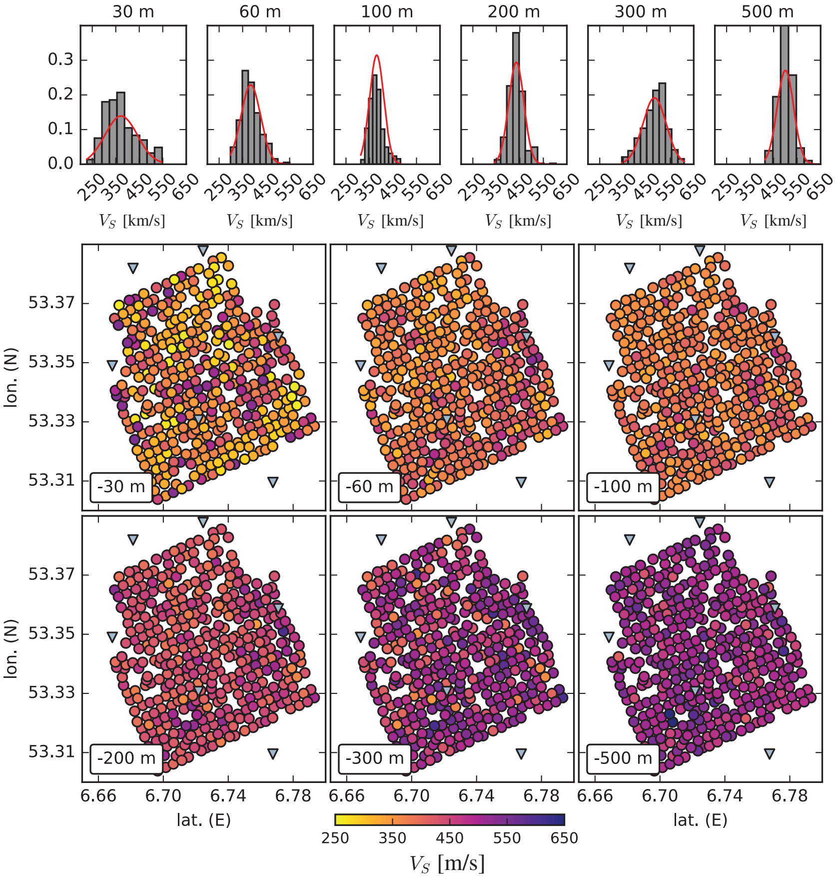

▲ **Figure 4.** Distribution of the velocities obtained from the 1D inversion at all locations and sorted by depth. The top panels depict the variability of the velocities as probability density functions. The other panels depict the variation of the velocities as a function of depth and as a function of station location.

In Figure 3, most of the spatial variability in the velocity model is observed in the upper ~200 m. Below that, the 1D models quickly evolve toward a gradient-like structure, as inferred in previous studies (Kruiver *et al.*, 2017; Spica, Perton, *et al.*, 2017). Interestingly, all velocity models in Figure 3 show an inversion of velocity in the first ~100 m. Because the harmonically averaged starting velocity model removes small velocity inversions in the velocity model of Kruiver *et al.* (2017), this feature is not related to the initial starting model. This feature has also previously been observed in the velocity models of Spica, Perton, *et al.* (2017). Numerical simulation shows that this velocity inversion leads to 20% amplification in the HVSR around 1 s when compared with the case where the velocity inversion is replaced by a gradient. This last point is potentially important for ground-motion prediction.

In Figure 4, we show the distribution of estimated velocities for the entire array at different depth levels (30, 60, 100, 200, 300, and 500 m). In the upper panels of Figure 4, we show the distribution of the velocity at each depth. From the lateral distribution of the velocities, we are not able to identify any clear geological structure at the scale of the array. Instead, we observe a scattered pattern of velocities from site to site, especially in the shallowest layers where the range of velocities is as large as a factor of 2 (Fig. 3). The variability then decreases with depth until 300 m, where it again increases. Several factors might contribute to this pattern. The topmost ~200 m of the Groningen area comprises thick layers of unconsolidated sediments that contain strong vertical and lateral heterogeneity (e.g., De Mulder *et al.*, 2003; Kruiver *et al.*, 2017). It is likely that the interstation distance of ~350 m is larger than the variability of the geological structures. We also note that our inversion scheme does not completely account for 3D structure. Although all inversions begin with the same starting velocity model, no physical smoothing is applied from station to station, which makes the inversions largely independent. Finally, the DCs obtained from azimuthally averaged FTAN sample frequencies ranging from ~1 to ~7 Hz are only weakly sensitive to depths greater than ~500 m (Spica *et al.*, 2018). For that reason, absolute velocities at depths deeper than ~500 m are likely not well constrained by our observations. That explains why the variability with depth increases again at 500 m. This characteristic is well observed in Figure 5, which shows all the velocity models obtained at each station and compared with other velocity models obtained independently for the Loppersum array. While the range of velocities and layer thickness is relatively low in the first ~500 m, these parameters vary much more at greater depth, suggesting much lower sensitivity of the method. The poor sensitivity of the parameters at these depths is due to the fact that HVSR only carries information below 1 Hz, and only weak constraints are added by the

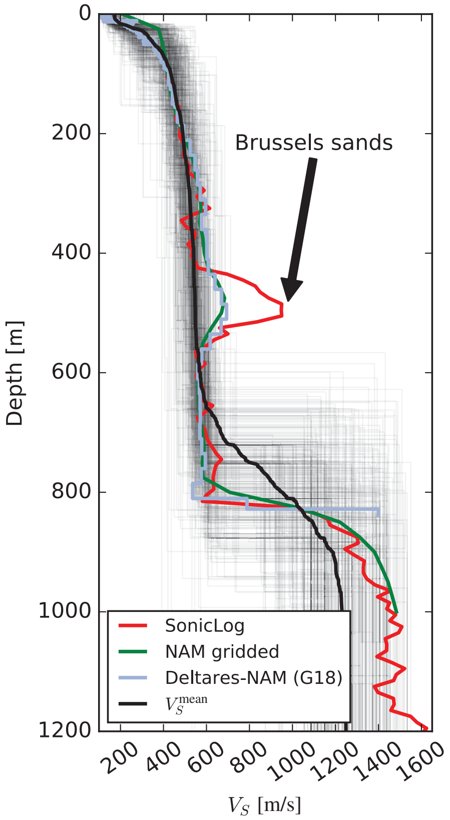

▲ **Figure 5.** Different velocity models obtained for the Loppersum array compared with the average velocity model obtained in this study (thick black line) and all velocity models obtained under each stations (tiny black lines). The Deltares-Nederlandse Aardolie Maatschappij (NAM) at shallow borehole site G18 is from Kruiver *et al.* (2017). The SonicLog velocity model was obtained at deep borehole SDM. The Deltares-NAM, SonicLog, and NAM-gridded velocity models are described in Kruiver *et al.* (2017).

DCs. A large range of solutions may then fit the observed HVSR acceptably well (e.g., Piña-Flores *et al.*, 2016); however, prior knowledge of the shallow structure tends to help mitigating the nonuniqueness of the solution. Although highly variable in each individual velocity model, the interface at ~800 m can still be approximated by considering the average velocity model from all the 1D inversions (thick black line in Fig. 5).

The averaged V_S model evolves gradually with depth and features a major step at the depth of the Lower North Sea Group and the Chalk Group interface. This contrast is not as sharp as in other velocity models, but velocities and average depth fit the other independent observations. This gradient-like characteristic in the first ~800 m is now well documented for the region and is also documented by the velocity distribution in the upper panel of Figure 4. This feature is also in agreement with the average shear-wave velocity versus depth for marine sediments (Hamilton, 1976) An evident discrepancy appears at about 500 m depth where the joint inversion does not retrieve the Brussels sands layer. While this layer appears with a strong velocity contrast in the SonicLog profile of the SDM (eastern) borehole (Fig. 1c), the contrast is much weaker in both the Kruiver *et al.* (2017) and in the NAM-gridded velocity model. This feature is likely not retrieved in our inversion due to the weak sensitivity of surface waves at these depths. Moreover, it is not well expressed in the HVSR measurements (i.e., no clear frequency peaks are observed in the data), which suggest it may be a weak feature under most of the Loppersum array. To enhance the sensitivity to the Brussels sands and the ~800 m velocity contrast in our inversion, one possibility would be to merge our high-frequency DCs with lower-frequency DCs obtained using larger-aperture subarrays. Overall, our analysis demonstrates that the joint inversion of local multimode surface-wave DCs along with full spectrum H/V can retrieve the major characteristics of the shallow structure and also some deeper features.

CONCLUSIONS

Based on a DFA, we computed multimode DCs for both Rayleigh and Love waves and also HVSR. We extracted DCs from cross correlation of ASF and HVSR from its autocorrelation. These three sets of measurements were inverted jointly to assess the 1D velocity structure at each of the 415 sites for a dense large-N temporary array. The joint use of these measurements helps reduce the degree of nonuniqueness.

The final product of this research is a new high-resolution shallow velocity model of the Loppersum area in the Groningen gas field province. Individual 1D velocity models share similar characteristics, especially in the first ~500 m. These include an inversion of velocity at about 100 m, a gradient velocity structure from ~200 to ~800 m, and a sharp velocity increase below. The inversion of velocity at ~100 m depth should be particularly relevant for ground-motion prediction. The average velocity profile agrees well with previous results for the Loppersum region. Although our analysis yields a single consistent structural picture of the near surface in agreement with the field data, it also highlights the large degree of vertical and lateral heterogeneity in the shallow subsurface. The next natural step for this study would be to integrate our results into path-dependent ground-motion prediction for the Groningen. For this reason, we provide along with this article in the Ⓔ electronic supplement the inverted velocity models obtained from the joint inversion at each station along with the average velocity model.

DATA AND RESOURCES

The data used in this study are the possession of Shell Global Solutions International B.V.

ACKNOWLEDGMENTS

We thank the staff of Nederlandse Aardolie Maatschappij (NAM), Royal Netherlands Meteorological Institute (KNMI), and Shell Global Solutions International B.V. for data acquisition, management, and distribution. We thank Pauline Kruiver from Deltares for providing us with their velocity models at borehole sites and Indrajit Das for providing us the data of the Loppersum array. This research was funded by Shell Global Solutions International B.V. All the figures have been plotted with Matplotlib, and some of the data processing steps have been performed using ObsPy (Hunter, 2007; Beyreuther *et al.*, 2010). The authors are grateful for the reviews of Matthew Haney, two anonymous reviewers, and for the editorial work of Editor-in-Chief Zhigang Peng and Brandon Schmandt.

REFERENCES

Arai, H., and K. Tokimatsu (2004). *S*-wave velocity profiling by inversion of microtremor H/V spectrum, *Bull. Seismol. Soc. Am.* **94,** no. 1, 53–63, doi: 10.1785/0120030028.

Bensen, G. D., M. H. Ritzwoller, M. P. Barmin, A. L. Levshin, F. Lin, M. P. Moschetti, N. M. Shapiro, and Y. Yang (2007). Processing seismic ambient noise data to obtain reliable broad-band surface wave dispersion measurements, *Geophys. J. Int.***169,** no. 3, 1239–1260, doi: 10.1111/j.1365-246X.2007.03374.x.

Berteussen, K. A. (1977). Moho depth determinations based on spectral-ratio analysis of NORSAR long-period *P* waves, *Phys. Earth Planet. In.* **15,** no. 1, 13–27, doi: 10.1016/0031-9201(77)90006-1.

Beyreuther, M., R. Barsch, L. Krischer, T. Megies, Y. Behr, and J. Wassermann (2010). ObsPy: A Python toolbox for seismology, *Seismol. Res. Lett.* **81,** no. 3, 530–533, doi: 10.1785/gssrl.81.3.530.

Bommer, J. J., P. J. Stafford, B. Edwards, B. Dost, E. van Dedem, A. Rodriguez-Marek, P. Kruiver, J. van Elk, D. Doornhof, and M. Ntinalexis (2017). Framework for a ground-motion model for induced seismic hazard and risk analysis in the Groningen gas field, the Netherlands, *Earthq. Spectra* **33,** no. 2, doi: 10.1193/082916EQS138M.

Bouchon, M. (2003). A review of the discrete wavenumber method, *Pure Appl. Geophys.* **160,** nos. 3/4, 445–465.

Brocher, T. M. (2005). Empirical relations between elastic wavespeeds and density in the Earth's crust, *Bull. Seismol. Soc. Am.* **95,** no. 6, 2081–2092.

Byrd, R. H., M. E. Hribar, and J. Nocedal (1999). An interior point algorithm for large-scale non-linear programming, *SIAM J. Optim.* **9,** no. 4, 877–900.

Campillo, M., S. K. Singh, N. M. Shapiro, J. Pacheco, and R. Herrmann (1996). Crustal structure of the Mexican volcanic belt, based on group velocity dispersion, *Geof. Int.* **35,** no. 4, 361–370.

Dal Moro, G. (2011). Some aspects about surface wave and HVSR analyses: A short overview and a case study, *Boll. Geof. Teor. Appl.* **52,** no. 2, doi: 10.4430/bgta0007.

De Mulder, E. F., M. C. Geluk, I. Ritsema, W. E. Westerhoff, and T. E. Wong (2003). *De ondergrond van Nederland*, Vol. 7, Wolters-Noordhoff, Groningen/Houten, The Netherlands, 379 (in Dutch).

Dziewonski, A., S. Bloch, and M. Landisman (1969). A technique for the analysis of transient seismic signals, *Bull. Seismol. Soc. Am.* **59,** no. 1, 427–444.

García-Jerez, A., J. Piña-Flores, F. J. Sánchez-Sesma, F. Luzón, and M. Perton (2016). A computer code for forward calculation and inversion of the H/V spectral ratio under the diffuse field assumption, *Comput. Geosci.* **97,** 67–78, doi: 10.1016/j.cageo.2016.06.016.

Hamilton, E. L. (1976). Shear-wave velocity versus depth in marine sediments: A review, *Geophysics* **41,** no. 5, 985–996.

Hofman, L., E. Ruigrok, B. Dost, and H. Paulssen (2017). A shallow seismic velocity model for the Groningen area in the Netherlands, *J. Geophys. Res.* **122,** doi: 10.1002/2017JB014419.

Hunter, J. D. (2007). Matplotlib: A 2D graphics environment, *Comput. Sci. Eng.* **9,** no. 3, 90–95, doi: 10.1109/MCSE.2007.55.

Jay, J. A., M. E. Pritchard, M. E. West, D. Christensen, M. Haney, E. Minaya, M. Sunagua, S. R. McNutt, and M. Zabala (2012). Shallow seismicity, triggered seismicity, and ambient noise tomography at the long-dormant uturuncu volcano, Bolivia, *Bull. Volcanol.* **74,** no. 4, 817–837.

Kruiver, P. P., E. van Dedem, R. Romijn, G. de Lange, M. Korff, J. Stafleu, J. L. Gunnink, A. Rodriguez-Marek, J. J. Bommer, J. van Elk, *et al.* (2017). An integrated shear-wave velocity model for the Groningen gas field, the Netherlands, *Bull. Earthq. Eng.* 1–26.

Lawrence, J. F., and G. A. Prieto (2011). Attenuation tomography of the western United States from ambient seismic noise, *J. Geophys. Res.* **116,** no. B06, 302.

Levshin, A. L., T. B. Yanovskaia, A. V. Lander, B. G. Bukchin, M. P. Barmin, L. I. Ratnikova, and E. N. Its (1989). Surface waves in vertically inhomogeneous media, in *Seismic Surface Waves in a Laterally Inhomogeneous Earth*, V. I. Keilis-Borok (Editor), Kluwer Academic Publisher, Nauka, Moscow, Russia, 3–33.

Lin, F.-C., M. P. Moschetti, and M. H. Ritzwoller (2008). Surface wave tomography of the western United States from ambient seismic noise: Rayleigh and Love wave phase velocity maps, *Geophys. J. Int.* **173,** no. 1, 281–298, doi: 10.1111/j.1365-246X.2008.03720.x.

Lin, F.-C., B. Schmandt, and V. C. Tsai (2012). Joint inversion of Rayleigh wave phase velocity and ellipticity using USArray: Constraining velocity and density structure in the upper crust, *Geophys. Res. Lett.* **39,** L12303, doi: 10.1029/2012GL052196.

Lontsi, A. M., M. Ohrnberger, F. Krüger, and F. J. Sánchez-Sesma (2016). Combining surface-wave phase-velocity dispersion curves and full microtremor horizontal-to-vertical spectral ratio for subsurface sedimentary site characterization, *Interpretation*, **4,** no. 4, SQ41–SQ49.

Lontsi, A. M., F. J. Sánchez-Sesma, J. C. Molina-Villegas, M. Ohrnberger, and F. Krüger (2015). Full microtremor H/V (z, f) inversion for shallow subsurface characterization, *Geophys. J. Int.* **202,** no. 1, 298–312.

Maraschini, M., F. Ernst, S. Foti, and L. V. Socco (2010). A new misfit function for multimodal inversion of surface waves, *Geophysics* **75,** no. 4, G31–G43.

Maupin, V. (2017). 3-d sensitivity kernels of the Rayleigh wave ellipticity, *Geophys. J. Int.* **211,** no. 1, 107–119.

Nakamura, Y. (1989). A method for dynamic characteristics estimation of subsurface using microtremor on the ground surface, *Q. Rep. Railway Tech. Res. Inst.* **30,** no. 1, 25–33.

Nakata, N., R. Snieder, S. Kuroda, S. Ito, T. Aizawa, and T. Kunimi (2013). Monitoring a building using deconvolution interferometry. I: Earthquake-data analysis, *Bull. Seismol. Soc. Am.* **103,** no. 3, 1662–1678.

Noorlandt, R., P. P. Kruiver, M. P. de Kleine, M. Karaoulis, G. de Lange, A. Di Matteo, J. von Ketelhodt, E. Ruigrok, B. Edwards, A. Rodriguez-Marek, *et al.* (2018). Characterisation of ground motion recording stations in the Groningen gas field, *J. Seismol.* 1–19, doi: 10.1007/s10950-017-9725-6.

Parolai, S., M. Picozzi, S. Richwalski, and C. Milkereit (2005). Joint inversion of phase velocity dispersion and H/V ratio curves from seismic noise recordings using a genetic algorithm, considering higher modes, *Geophys. Res. Lett.* **32,** L01303, doi: 10.1029/2004GL021115.

Perton, M., and F. J. Sánchez-Sesma (2014). *Normalization during the Processing of Noise Correlations*, IUGG, Merida, Mexico.

Perton, M., and F. J. Sánchez-Sesma (2016). Green's function calculation from equipartition theorem, *J. Acoust. Soc. Am.* **140,** no. 2, 1309–1318.

Perton, M., F. J. Sánchez-Sesma, A. Rodrguez-Castellanos, M. Campillo, and R. L. Weaver (2009). Two perspectives on equipartition in diffuse elastic fields in three dimensions, *J. Acoust. Soc. Am.* **126,** no. 3, 1125–1130, doi: 10.1121/1.3177262.

Perton, M., Z. Spica, and C. Caudron (2017). Inversion of the horizontal-to-vertical spectral ratio in presence of strong lateral heterogeneity, *Geophys. J. Int.* **212,** no. 2 930–941, doi: 10.1093/gji/ggx458

Piña-Flores, J., M. Perton, A. García-Jerez, E. Carmona, F. Luzón, J. C. Molina-Villegas, and F. J. Sánchez-Sesma (2016). The inversion of spectral ratio H/V in a layered system using the diffuse field assumption (DFA), *Geophys. J. Int.* **208,** doi: 10.1093/gji/ggw416.

Rivet, D., M. Campillo, F. Sánchez-Sesma, N. M. Shapiro, and S. K. Singh (2015). Identification of surface wave higher modes using a methodology based on seismic noise and coda waves, *Geophys. J. Int.* **203,** no. 2, 856–868.

Rodriguez-Marek, A., P. P. Kruiver, P. Meijers, J. J. Bommer, B. Dost, J. van Elk, and D. Doornhof (2017). A regional site-response model for the Groningen gas field, *Bull. Seismol. Soc. Am.* **107,** no. 5, 2067–2077.

Sabra, K. G., P. Gerstoft, P. Roux, W. A. Kuperman, and M. C. Fehler (2005). Surface wave tomography from microseisms in southern California, *Geophys. Res. Lett.* **32,** no. 14, L14311, doi: 10.1029/2005GL023155.

Salinas, V., F. Luzón, A. García-Jerez, F. Sánchez-Sesma, H. Kawase, S. Matsushima, M. Suarez, A. Cuellar, and M. Campillo (2014). Using diffuse field theory to interpret the H/V spectral ratio from earthquake records in Cibeles seismic station, Mexico City, *Bull. Seismol. Soc. Am.* **104,** no. 2, 995–1001.

Sánchez-Sesma, F. J., M. Rodrguez, U. Iturrarán-Viveros, F. Luzón, M. Campillo, L. Margerin, A. García-Jerez, M. Suarez, M. A. Santoyo, and A. Rodrguez-Castellanos (2011). A theory for microtremor H/V spectral ratio: Application for a layered medium, *Geophys. J. Int.* **186,** no. 1, 221–225, doi: 10.1111/j.1365-246X.2011.05064.x.

Scherbaum, F., K.-G. Hinzen, and M. Ohrnberger (2003). Determination of shallow shear wave velocity profiles in the Cologne, Germany area using ambient vibrations, *Geophys. J. Int.* **152,** no. 3, 597–612.

Shapiro, N. M., and M. Campillo (2004). Emergence of broadband Rayleigh waves from correlations of the ambient seismic noise, *Geophys. Res. Lett.* **31,** no. 7, doi: 10.1029/2004GL019491.

Shapiro, N. M., M. Campillo, L. Stehly, and M. H. Ritzwoller (2005). High-resolution surface-wave tomography from ambient seismic noise, *Science* **307,** no. 5715, 1615–1618, doi: 10.1126/science.1108339.

Spica, Z., C. Caudron, M. Perton, T. Lecocq, T. Camelbeeck, D. Legrand, J. Piña-Flores, A. Iglesias, and D. K. Syahbana (2015). Velocity models and site effects at Kawah Ijen volcano and Ijen caldera (Indonesia) determined from ambient noise cross-correlations and directional energy density spectral ratios, *J. Volcanol. Geoth. Res.* **302,** 173–189, doi: 10.1016/j.jvolgeores.2015.06.016.

Spica, Z., D. Legrand, A. Iglesias, T. R. Walter, H. Sebastian, T. Dahm, J.-L. Froger, D. Rémy, S. Bonvalot, and M. Pardo (2015). Hydrothermal and magmatic reservoirs at Lazufre volcanic area, revealed by a high-resolution seismic noise tomography, *Earth Planet. Sci. Lett.* **421,** 27–38, doi: 10.1016/j.epsl.2015.03.042.

Spica, Z., M. Perton, and G. C. Beroza (2017). Lateral heterogeneity imaged by small-aperture ScS retrieval from the ambient seismic field, *Geophys. Res. Lett.* **44,** no. 16, 8276–8284, doi: 10.1002/2017GL073230.

Spica, Z., M. Perton, M. Calò, D. Legrand, F. Córdoba-Montiel, and A. Iglesias (2016). 3-D shear wave velocity model of Mexico and south US: Bridging seismic networks with ambient noise cross-correlations (C^1) and correlation of coda of correlations (C^3), *Geophys. J. Int.* **206,** no. 3, 1795–1813, doi: 10.1093/gji/ggw240.

Spica, Z., M. Perton, and D. Legrand (2017). Anatomy of the Colima volcano magmatic system, Mexico, *Earth Planet. Sci. Lett.* **459,** 1–13, doi: 10.1016/j.epsl.2016.11.010.

Spica, Z. J., N. Nakata, X. Liu, T. Zijian, X. Campman, and G. C. Beroza (2018). The ambient seismic field at Groningen gas field: An overview from the surface to reservoir depth, *Seismol. Res. Lett.* doi: 10.1785/0220170256

Spica, Z. J., M. Perton, N. Nakata, X. Liu, and G. C. Beroza (2017). Site characterization at Groningen gas field area through joint surface-borehole H/V analysis, *Geophys. J. Int.* **212,** no. 1, 412–421, doi: 10.1093/gji/ggx426.

Stankiewicz, J., M. H. Weber, A. Mohsen, and R. Hofstetter (2012). Dead sea basin imaged by ambient seismic noise tomography, *Pure Appl. Geophys.* **169,** no. 4, 615–623, doi: 10.1007/s00024-011-0350-y.

Tomar, G., E. Stutzmann, A. Mordret, J.-P. Montagner, S. C. Singh, and N. M. Shapiro (2018). Joint inversion of the first overtone and fundamental mode for deep imaging at the Valhall oil field using ambient noise, *Geophys. J. Int.*, **214,** no. 1, 122–132, doi: 10.1093/gji/ggy122

van Elk, J., D. Doornhof, J. J. Bommer, S. J. Bourne, S. J. Oates, R. Pinho, and H. Crowley (2017). Hazard and risk assessments for induced seismicity in Groningen, Netherlands, *J. Geosci.* **96,** no. 5, s259–s269.

van Thienen-Visser, K., and J. Breunese (2015). Induced seismicity of the Groningen gas field: History and recent developments, *The Leading Edge* **34,** no. 6, 664–671.

Wu, H., K. Masaki, K. Irikura, and F. J. Sánchez-Sesma (2017). Application of a simplified calculation for full-wave microtremor H/V spectral ratio based on the diffuse field approximation to identify underground velocity structures, *Earth Planets Space* **69,** no. 1, 162, doi: 10.1186/s40623-017-0746-8.

Zhou, W., and H. Paulssen (2017). *P* and *S* velocity structure in the Groningen gas reservoir from noise interferometry, *Geophys. Res. Lett.* **44,** no. 23, 11,785-11,791, doi: 10.1002/2017GL075592.

Zor, E., S. Özalaybey, A. Karaaslan, M. C. Taprdamaz, S. Ç. Özalaybey, A. Tarancoğlu, and B. Erkan (2010). Shear wave velocity structure of the Izmit Bay area (Turkey) estimated from active–passive array surface wave and single-station microtremor methods, *Geophys. J. Int.* **182,** no. 3, 1603–1618.

Zack Spica
Xin Liu
Gregory C. Beroza
Department of Geophysics
Stanford University
397 Panama Mall
Stanford, California 94305-2215 U.S.A.
zspica@stanford.edu

Mathieu Perton
CONACYT
Instituto de Geofísica UNAM, Unidad Michoacán
Antigua Carretera a Pátzcuaro 8701
58190 Morelia, Michoacán
Mexico

Nori Nakata
ConocoPhillips School of Geology and Geophysics
University of Oklahoma
Norman, Oklahoma U.S.A.